Synthesis of solid solutions of $Cd_{1-x}Zn_xS$ nanocrystals in the channels of mesostructured silica films

Yaşar Akdoğan,[a] Çağrı Üzüm,[a] Ömer Dag*[a] and Neil Coombs[b]

Received 20th February 2006, Accepted 29th March 2006
First published as an Advance Article on the web 21st April 2006
DOI: 10.1039/b602584f

In this contribution, we introduce the use of metal ion (Cd(II) and Zn(II)) modified mesostructured silica as a reaction medium, to produce a solid solution of $Cd_{1-x}Zn_xS$ nanocrystals as a thin film. With this approach, a true liquid crystalline templating (TLCT) and liquid crystalline mesophase of transition metal salt : oligo(ethylene oxide) non-ionic surfactant ($((1-x)[Cd(H_2O)_4](NO_3)_2 + x[Zn(H_2O)_6](NO_3)_2) : CH_3(CH_2)_{11}(OCH_2CH_2)_{10}OH$, (MLC)), systems were collectively used to synthesise mesostructured silica films. The film samples were reacted at room temperature (RT) in an H_2S atmosphere to produce zinc blend $Cd_{1-x}Zn_xS$ nanocrystals in the channels of mesostructured silica. The initial Zn(II) and Cd(II) ion concentrations in the reaction media determine the final composition and band gap of the $Cd_{1-x}Zn_xS$ nanocrystals. The growth process of the $Cd_{1-x}Zn_xS$ nanocrystals in the pores is influenced by the silica walls. If the walls are rigid (well polymerized, obtained by aging the samples before H_2S treatment), then the $Cd_{1-x}Zn_xS$ nanoparticles are smaller in size and more uniform in size distribution.

Introduction

The modification of the internal surface of existing mesoporous materials[1] and the synthesis of new mesostructured materials with optical, magnetic and catalytic components are emerging fields in materials chemistry.[2–10] Mesoporous materials have regular and tunable pores with large surface areas. Modifying the surface with optical, magnetic and catalytic materials will prove beneficial in various applications. There are many methods described in the literature for modifying the surface of mesoporous materials with active materials. Chemical vapor deposition,[6] ion-exchange[7,8] impregnation,[9,10] true liquid crystalline templating (TLCT),[11,12] functionalizing the pore walls with organic groups to incorporate various nanocrystals into the pores,[13] doping mesopores with quantum dots,[14] *etc.* are some examples of the methods. Using various approaches, CdS, ZnS, $Zn_{1-x}Mn_xS$, and $Cd_{1-x}Mn_xS$ nanoparticles have also been synthesized in the channels of mesoporous silica.[7–10,12,15–18]

In this article, we focus on the TLCT approach that uses C_nEO_m non-ionic surfactants in a lyotropic liquid crystalline (LLC) mesophase as the templating agent.[11] A mixture of surfactant, acid (as a catalyst), tetramethylorthosilicate (TMOS, as silica source) and water first produces a liquid mixture that undergoes a transformation, with hydrolysis and condensation, of the silica source to form an LC mesophase and then with further polymerization a solid phase. Mesostructured metal sulfides[19–21] and metals[22,23] have also been synthesized using the TLCT approach. As an extension to the use of the LLC mesophase, we have introduced a new metal ion containing liquid crystalline (MLC) mesophase[24,25] that consists of transition metal salts (TMS) and non-ionic surfactants, C_nEO_m. The MLC mesophase can be used in the context of TLCT to introduce transition metal ions into mesostructured silica in a one pot synthesis.[12] The method described here is quite flexible in that more than one type of transition metal ion can be incorporated at once. This is an important step in incorporating optical and magnetic components into wide band gap semiconductors in the channels of the mesostructured materials in one pot. Furthermore, the structure of the MLC mesophase can be controlled using the salt concentration, ionic strength and the type of counter anion in the medium.[12,25] For example, the nitrate salts of TMS with C_nEO_m produce a 2D hexagonal mesophase, however introducing about 10% water changes the structure to a 3D hexagonal mesophase and further increases in the water concentration produce a micelle solution.[25] The perchlorate salts usually produce cubic mesophases.[25] Combining the TLCT approach with the MLC mesophase has the advantage in that it enhances the structural and component flexibility of the final materials.

$Cd_{1-x}Zn_xS$ are direct gap semiconductor materials that are promising for high density optical recording, blue or even UV laser diodes.[26,27] The solid-solution behavior of $Cd_{1-x}Zn_xS$ nanocrystals has been observed in various media.[28–31] The band gap of $Cd_{1-x}Zn_xS$ has an almost linear dependence on the composition, x, and can be tuned between the band gaps of the CdS and ZnS materials.[28,29] The particle size also plays an important role in determining the band gap of the final materials due to the quantum confinement effect.[32]

In this contribution, the mesostructured silica materials modified with $Cd_{1-x}Zn_xS$ nanoparticles were characterized

[a]*Laboratory for Advanced Functional Materials, Department of Chemistry, Bilkent University, 06800, Ankara, Turkey. E-mail: dag@fen.bilkent.edu.tr; Fax: +90-312-266-4579; Tel: +90-312-266-3918.*
[b]*Centre for Nanostructure Imaging, Lash-Miller Building, Department of Chemistry, 80 St. George St., University of Toronto, M5S 3H6, On., Canada*

using UV-Vis absorption (in transmittance mode), XRD method, POM and TEM microscopy techniques.

Experimental

Synthesis of $Cd_{1-x}Zn_xS$ in mesostructured silica

Various amounts, $1 - x$ (0.493 to 0.0 g) and x (0.0 to 0.475 g) of the $[Cd(H_2O)_4](NO_3)_2$ and $[Zn(H_2O)_6](NO_3)_2$ salts, respectively, were dissolved in 3 ml of H_2O that was acidified using 0.10 g of concentrated nitric acid (70%). To this mixture, first 1.00 g of $C_{12}EO_{10}$ and then 1.60 g of TMOS were added at once. Either gentle heating or simple shaking homogenized the resulting liquid mixture. The film samples were prepared by dip coating with a coating speed of 0.4 mm s^{-1} over glass, quartz and silicon surfaces for various measurements. The Cd^{2+} and Zn^{2+} containing mesostructured materials were prepared by varying the Zn^{2+} mole fraction from 0.0 to 1.0 and with a $M^{2+}/C_{12}EO_{10}$ (M^{2+} is the total number of Zn^{2+} and Cd^{2+} ions) mole ratio of 1.0. Then, the film samples were reacted in an evacuated reaction chamber under 50–150 Torr of H_2S gas. This process usually produces stable transparent nano$Cd_{1-x}Zn_xS$–mesoSiO_2 composite materials. Some of the film samples were aged before H_2S reaction at various temperatures (between RT and 240 °C) by slow heating (for 45 minutes) and heating at the desired temperature for a certain period of time (see Results and discussion).

Characterization

Polarized optical microscopy (POM) images were obtained in transmittance mode on a Meije Techno ML9400 series Polarising Microscope with transmitted light illumination, using convergent white light between the parallel and crossed polarizer. X-Ray diffraction (XRD) patterns were recorded on a Rigaku Miniflex diffractometer using a high power Cu-K_α source operating at 30 kV and 15 mA. The XRD patterns were recorded in low and high angle regions to monitor both the mesophase and $Cd_{1-x}Zn_xS$ nanocrystals, respectively. UV-Vis spectra were recorded using a Varian Cary 5 double beam spectrophotometer with 150 nm min^{-1} speed with a resolution of 2 nm over a wavelength range from 700 to 200 nm in transmittance mode. The UV-Vis absorption spectra were obtained from the film samples of nano$Cd_{1-x}Zn_xS$–mesoSiO_2 materials. TEM images were recorded on a Hitachi HD-2000 STEM operating at 200 kV and 30 mA and a Philips 430 microscope with an accelerating voltage of 100 kV. The samples were prepared by dispersing the powder/fragments onto a carbon film-supported 200 mesh copper grid or embedded in epoxy resin and microtome. ^{29}Si MAS-NMR (magic angle spinning nuclear magnetic resonance) proton coupled spectra were recorded using a Bruker DSX 400 spectrometer with a recycle delay time of 100 s. Samples were spun at 5000 Hz, the chemical shift values were reported with respect to tetramethylsilane.

Results and discussion

The hydrolysis and condensation of tetramethylorthosilicate (TMOS, 1.6 g) in a solution of water, nitric acid and $C_{12}H_{25}(OCH_2CH_2)_{10}OH$ (denoted C_nEO_m) with compositions of 3.0 g : 0.1 g : 1.0 g, respectively, produce a liquid crystalline mesophase that transforms to mesostructured silica over time. Adding a certain amount of metal salt into the above mixture does not interrupt the process. However, the salt concentration and salt type influence the structure of the silicatropic LC mesophase (and as a result, the structure of the silica materials).[12] At low salt concentrations (0.0 to 1.0 salt/surfactant mole ratios), the silicatropic LC mesophase (in early stages) and mesostructured silica (after aging the mixture for several hours) have hexagonal structures that change to cubic structures at higher salt concentrations.[12] The same change happens at a much lower concentration of perchlorate salts. Note also that the mesophase is disordered in a $[M(H_2O)_6](NO_3)$: $C_{12}EO_{10}$ system at salt/surfactant mole ratios between 0.0 and 1.0.[23] However, the $[M(H_2O)_6](NO_3)$: $C_{12}EO_{10}$ binary mixtures have a 2D hexagonal mesophase at salt/surfactant mole ratios between 1.2 and 3.2.[23] Therefore, the silica species that is forming in the early stages in the reaction medium behave similarly to the salt ions and organize the surfactant molecules into a LC mesophase and eventually into mesostructured silica materials.

This work focuses on mixed salt systems (where salts are $[Cd(H_2O)_4](NO_3)_2$ and $[Zn(H_2O)_4](NO_3)_2$) with a medium salt concentration (total salt/surfactant mole ratio of 1.0), where the mesostructured silica film is ordered.[12] The film samples (represented as $Cd(II)_{1-x}Zn(II)_x$–mesoSiO_2) were prepared by varying the Zn^{2+} mole fraction, x, between 0.0 and 1.0 with increments of 0.1. Fig. 1 shows a typical POM image of a relatively thick film sample. Note that the film samples in all compositions are birefringent between the crossed polarizers. The POM images display similar schlieren textures, characteristic of the columnar structures (see Fig. 1). Fig. 2 shows a series of XRD patterns recorded from the film samples. All the film samples display similar X-ray diffraction patterns between 1.0 and 5.0° 2θ, characteristic of oriented mesostructured silica (one very strong line at around 1.77° and a very weak one at 3.50° 2θ).[33] However, crushed samples obtained from thicker films and/or monoliths display up to 4 diffraction lines at 1.77°, 2.00°, 2.48°, and 2.91° 2θ.

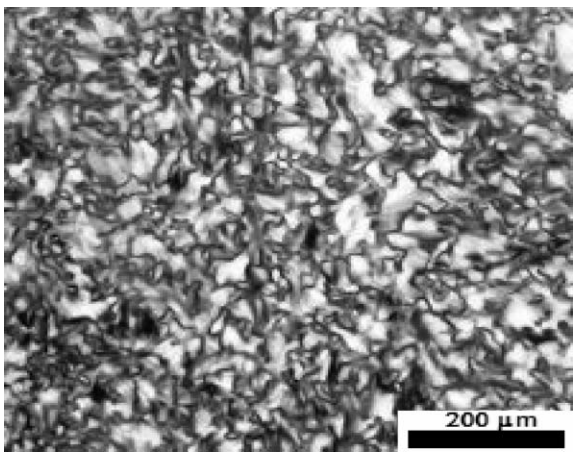

Fig. 1 A typical polarized optical microscopy image of a $[Cd(H_2O)_4](NO_3)_2$–mesoSiO_2 thick film.

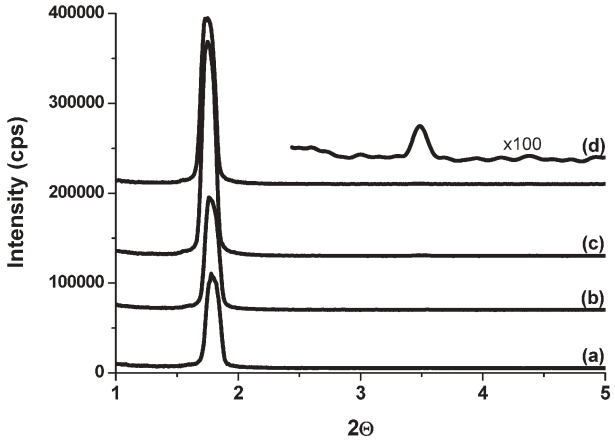

Fig. 2 The XRD patterns of the film samples of a) $[Cd(H_2O)_4](NO_3)_2$–mesoSiO$_2$, b) $(Cd(II))_{0.7}(Zn(II))_{0.3}$–mesoSiO$_2$, c) $(Cd(II))_{0.4}(Zn(II))_{0.6}$–mesoSiO$_2$ and d) $[Zn(H_2O)_6](NO_3)_2$–mesoSiO$_2$.

Yu *et al.*[34] have extensively investigated the structures of mesostructured silica monoliths and films, which were obtained using P123, $(PEO)_{20}(PPO)_{70}(PEO)_{20}$ (EO = $–CH_2CH_2O–$ and PO = $–CH(CH_3)CH_2O–$). They found that the thin films (300–500 nm thick) have 2D hexagonal mesostructures (*P6m*), while the monoliths have centered rectangular structures (*Cmm*) under similar conditions.[34] The hydrothermal treatment of the as-synthesized sample with *Cmm* structure results in structural evolution into the more stable *P6m* structure.[34] Our thicker samples and monoliths display diffraction lines of a columnar rectangular mesostructure, Fig. 3(A) and (B). The lines observed at 1.77, 2.00, 2.48, and 2.91° 2θ correspond to the (11), (20) (21), and (02) planes, respectively, of a columnar 2D rectangular structure. Since the (21) line is observed, the space group is *P2gg* rather than *Cmm*. Note that the $(h + k) = 2n + 1$ lines are forbidden ($(h + k) = 2n$ are the allowed diffraction planes) in the *C2mm* space group.[35] The unit cell parameters (a = 88.2 Å and b = 60.3 Å, with a/b = 1.4635) and the plot of the d-spacing *versus* the *hk* relation, obtained from $1/d^2 = h^2/a^2 + k^2/b^2$, are consistent with the 2D rectangular structure. Note also that Yu *et al.*[34] described samples with a/c ratio less than 1.77 as unstable; they transform to a 2D hexagonal structure. The diffraction line represented with an asterisk at 2.20° 2θ may correspond to the 2D hexagonal structure, which co-exists in the monoliths with the 2D rectangular structure. Note also that a similar transformation was observed in the P123 mesostructured silica systems.[34] It appears that in our monoliths we have a mixture of both phases.

However, the film samples display a very strong diffraction line at around 1.77° 2θ that is extremely sensitive to aging. The aging of the films was systematically investigated between RT and 240 °C to optimize the conditions in which the transparent film samples are prepared. The film samples were heated in a temperature controlled oven under laboratory conditions from RT to the desired temperature for 45 minutes and kept at this temperature from 30 minutes to 3 days. The aging gradually increases the silica condensation (silanol, –SiOH, groups into –SiOSi–, see NMR section below) and shrinks the silica walls to make the silica walls more rigid. For example, the

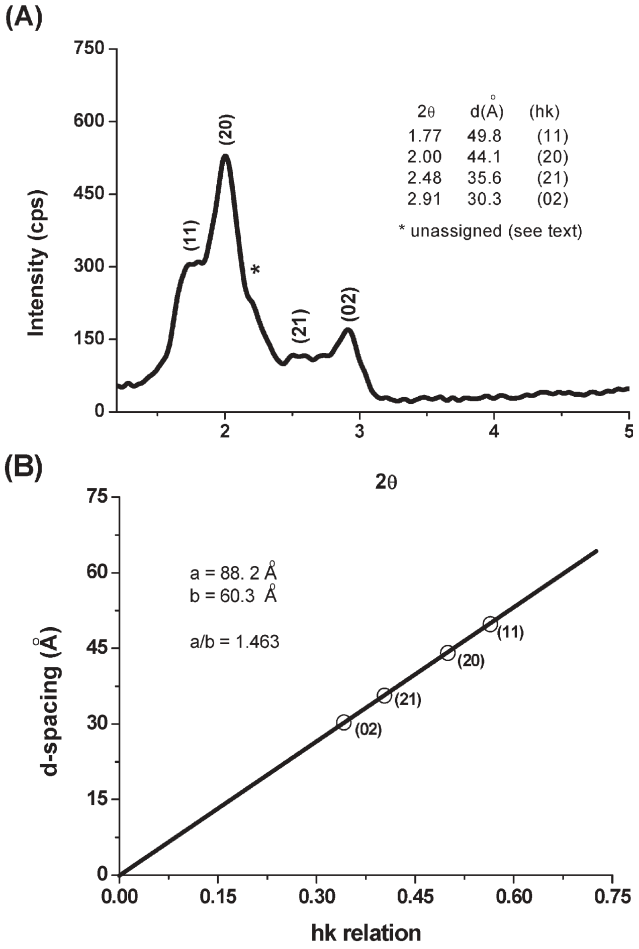

Fig. 3 (A) XRD pattern of a monolith (thicker film) of $[Cd(H_2O)_4](NO_3)_2$–mesoSiO$_2$ crashed into powder. (B) Plot of d-spacing obtained from (A) *versus hk* relation obtained from ($1/d^2 = h^2/a^2 + k^2/b^2$).

diffraction line shifts from 1.77° to 1.88° and to 2.38° 2θ upon aging at 100 °C for 2 hours and at 240 °C for 2 hours, respectively, Fig. 4. Notice also that there is a deviation from the trend of the shifts at 240 °C; this is most likely due to the burning of the surfactant molecules at around 240 °C. Aging the samples at each temperature for a longer duration shifts the diffraction line to an even higher angle at each temperature. For example, this line shifts up to 2.57° 2θ at 240 °C aging for 1 day. The aging process was also followed using ^{29}Si NMR spectroscopy. The ^{29}Si MAS-NMR spectra of the samples display 3 peaks at δ −91, −101, and −110 ppm with respect to tetramethylsilane due to $Si(OH)_2(OSi)_2$ (Q_2), $Si(OH)(OSi)_3$ (Q_3) and $Si(OSi)_4$ (Q_4) units, respectively. The trend in the spectra shows that the Q_4 band at −110 ppm increases in intensity with increasing aging temperature, indicating further condensation of the silanol groups.

The fresh and aged samples were exposed to an H_2S atmosphere in a closed evacuated reaction chamber to convert all Cd(II) and Zn(II) metal ions ($(Cd(II)_{1-x}Zn(II)_x$–mesoSiO$_2$) into $Cd_{1-x}Zn_xS$ in the silica channels (represented as nano$Cd_{1-x}Zn_xS$–mesoSiO$_2$). The EDX elemental analysis of the H_2S treated samples and their initial salt concentrations in

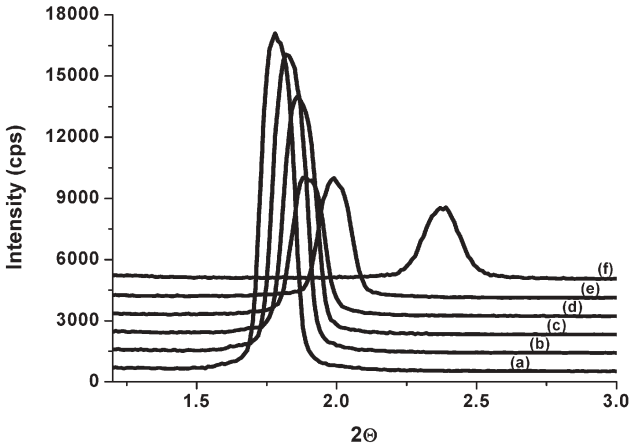

Fig. 4 The changes in XRD pattern of the $[Cd(H_2O)_4](NO_3)_2$–$mesoSiO_2$ film sample after ageing for 2 hours at (a) RT, (b) 50 °C, (c) 100 °C, (d) 150 °C, (e) 200 °C, and (f) 240 °C. Note that the XRD patterns were recorded by blocking the detector (to protect detector from the high intensity X-ray beam) with a thin copper block, which reduces the intensity about 10 times.

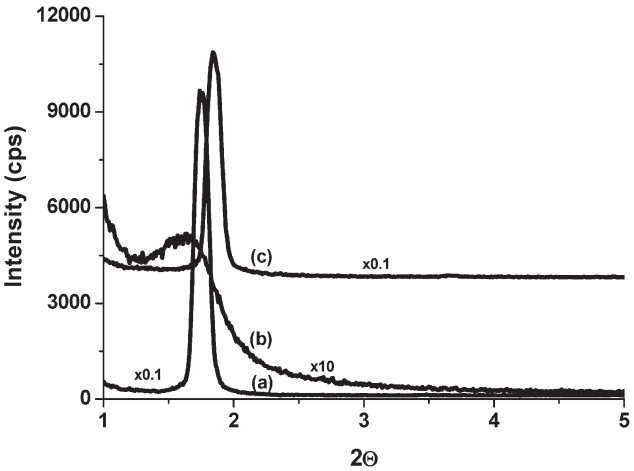

Fig. 5 The XRD patterns of (a) $[Zn(H_2O)_6](NO_3)_2$–$mesoSiO_2$ aged up to 4 hours at RT, (b) nanoZnS–$mesoSiO_2$ obtained from the sample in (a) by reacting under H_2S and (c) nanoZnS–$mesoSiO_2$ obtained after 1 day aging at RT and then reacted under H_2S atmosphere.

the mesostructured silica correlate with each other. The metal ion/sulfur mole ratio after the H_2S reaction is obtained from EDX measurements to be around 1.0 in all samples, also indicating the formation of the $Cd_{1-x}Zn_xS$ particles in the mesostructured silica matrix.

The sharp diffraction line at around 1.77° (49.9 Å) shifts to 1.58° (55.9 Å) and becomes broader in the fresh samples, indicating an enlargement of the silica repeating distances (due to the soft nature of partially polymerized silica walls) and disorder in the pores, and/or the formation of $Cd_{1-x}Zn_xS$ nanoparticles in the channels, respectively, Fig. 5. However, the aged samples do not show any shift or broadening with the H_2S reaction, indicating that the silica walls are quite rigid and limit the growth of the $Cd_{1-x}Zn_xS$ nanoparticles, Fig. 5. Note also that the samples aged at RT for 1 day or more and the samples aged at higher temperatures become resistant to the growth of the $Cd_{1-x}Zn_xS$ nanocrystals.

Fig. 6 and 7 display TEM images of the fresh and aged film samples upon the H_2S reaction. The images show channels in the mesostructured silica and nanocrystals of $Cd_{1-x}Zn_xS$ in the channels after H_2S treatments. The oriented channels and channel dimensions are consistent with the XRD results. Fig. 6(A) shows a dark field image of a portion of a relatively thicker modified silica particle of a fresh 1 : 1 Cd(II) and Zn(II) sample, which was reacted under H_2S gas, indicating spots (aggregates) of $Cd_{0.5}Zn_{0.5}S$ nanoparticles. The image in Fig. 6(B) clearly shows that these spots consist of ultra-small nanoparticles (see also discussion on UV-Vis absorption spectroscopy and XRD). The changes in the XRD pattern in the small angle regions after the H_2S treatment (Fig. 5) and the TEM image in Fig. 6(A) (aggregation) collectively show that the $Cd_{1-x}Zn_xS$ nanoparticles are forming inside the silica channels and are causing an enlargement of the silica pores in the fresh film samples. However, the aged samples display unaltered, sharp diffraction lines before and after the H_2S reaction. The TEM images in Fig. 7 also show that the nanoparticles are homogeneously distributed with a uniform size distribution in the silica matrix in the aged samples.

The XRD pattern in the high angle region displays changes depending on the Zn(II)/Cd(II) ratios of the $[M(H_2O)_n](NO_3)_2$–$mesoSiO_2$ upon H_2S treatment, Fig. 8(A). The high angle regions of the diffraction patterns were recorded using relatively thicker film samples, which were prepared on silicon wafers to improve the signal to noise ratio. The Si (200) line observed at 32.96° 2θ was used as an external reference to obtain the unit cell parameters of the $Cd_{1-x}Zn_xS$ nanocrystals. The (111), (220) and (311) diffraction lines of the zinc blend structure of the $Cd_{1-x}Zn_xS$ nanocrystals are observed at

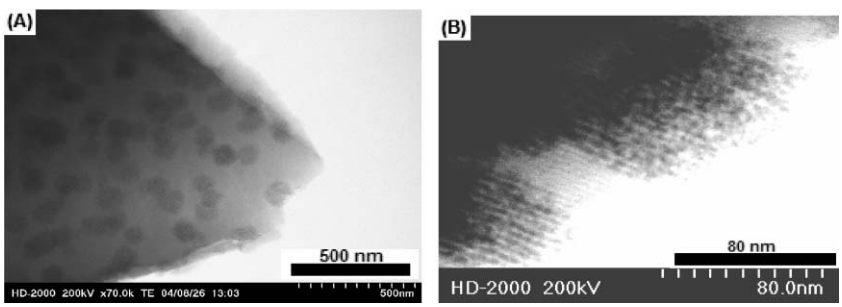

Fig. 6 The dark field TEM images of a fresh nano$Cd_{0.5}Zn_{0.5}S$–$mesoSiO_2$ film sample: (A) a thicker part of the sample and (B) a thinner section of the same sample.

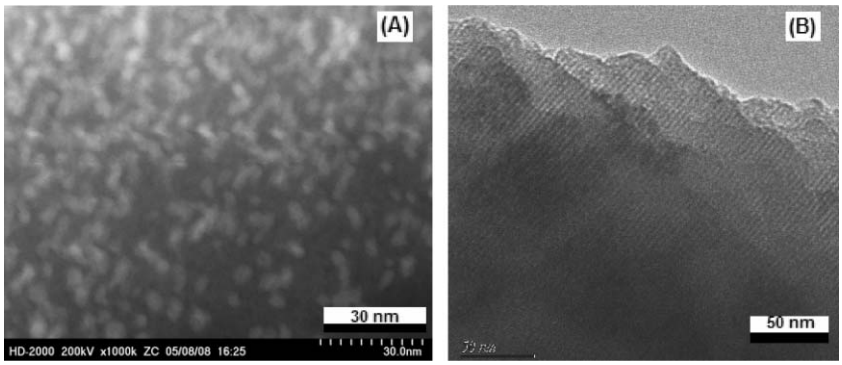

Fig. 7 The TEM images of the aged (at 100 °C for 2 hours) film samples of nano$Cd_{0.3}Zn_{0.7}S$–mesoSiO_2: (A) a bright field image of a relatively thick sample and (B) a dark field image of a thinner cross section of another sample prepared under the same conditions.

around 26.40, 44.00 and 52.60° 2θ, respectively, from the nanoCdS–mesoSiO_2. These diffraction lines gradually shift to higher angles going from CdS to ZnS in the $Cd_{1-x}Zn_xS$ nanocrystals, Fig. 8(A). The unit cell parameter, a, for the zinc blend structure correlates well with the composition, x, Fig. 8(B). The linear dependence of the unit cell parameter on the composition clearly indicates that the nanocrystals are forming a solid solution in the nano$Cd_{1-x}Zn_xS$–mesoSiO_2 films and monoliths.

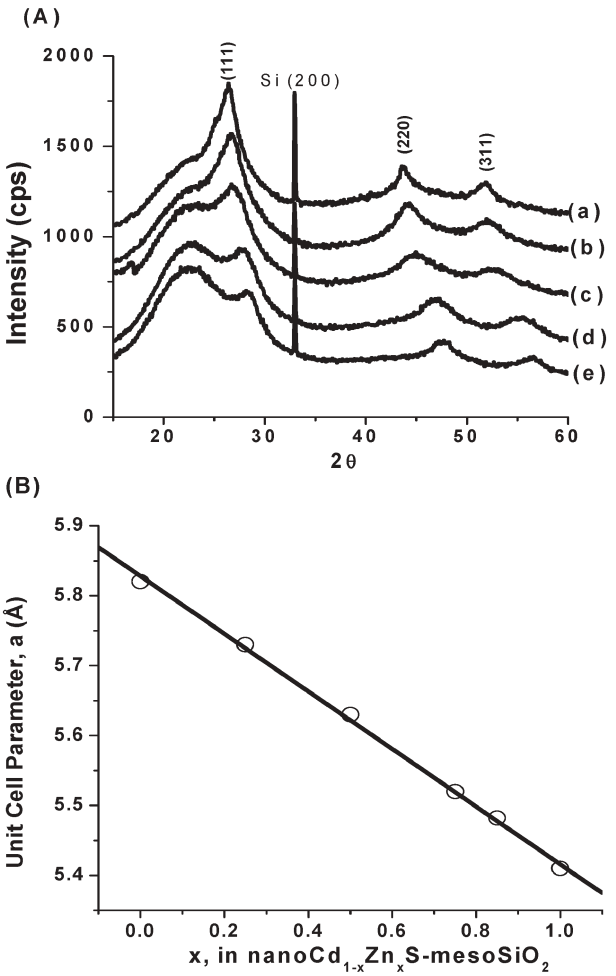

Fig. 8 The XRD patterns of nano$Cd_{1-x}Zn_xS$–mesoSiO_2 of mesostructured silica films, where x is (a) 0.00, (b) 0.25, (c) 0.50, (d) 0.85 and (e) 1.00. The sharp line at 32.96° is from the Si substrate (used as an internal reference). (B) A plot of the unit cell parameter, a, of the $Cd_{1-x}Zn_xS$ nanocrystallites (evaluated from the XRD patterns in (A)) *versus* composition, x, in nano$Cd_{1-x}Zn_xS$–mesoSiO_2.

The UV-Vis absorption spectra were recorded in transmittance mode for all film samples, Fig. 9(A), to elucidate the electronic properties of the nanocrystallites as well as to characterize them. The low energy absorption edge gradually blue shifts going from nanoCdS–mesoSiO_2 to nanoZnS–mesoSiO_2 film samples. The band gaps for each sample were evaluated using the linear fit of the absorption edge after plotting the spectra against the direct gap relationship, $(Ahv)^2$ *versus* hv (where A is absorbance and hv is the energy in eV). The variation of the band gaps (from 2.63 eV in x = 0.0 to 4.05 eV in x = 1.0) of nano$Cd_{1-x}Zn_xS$–mesoSiO_2 with x is shown in Fig. 9(B). Note that the blue shift from the bulk E_g values, by 0.21 and 0.37 eV for the two end compositions CdS and ZnS, respectively, indicates that the particles are smaller at the Zn(II) rich end of the $Cd_{1-x}Zn_xS$ nanocrystals. This observation is consistent with the XRD patterns, in which the diffraction lines are broader at the Zn(II) rich end of the $Cd_{1-x}Zn_xS$ nanocrystals. The variation of the E_g of the nano$Cd_{1-x}Zn_xS$–mesoSiO_2 with x fits an empirical quadratic relation ($E_g = 2.67 + 0.54x + 0.82x^2$). A similar dependence in the microcrystalline bulk $Cd_{1-x}Zn_xS$ crystals ($E_g = 2.42 + 0.9x + 0.3x^2$) with a different bowing parameter has been reported.[36] The two ends of the series, the Cd(II) rich and Zn(II) rich ends, show extra deviations, most likely due to the variation in particle size.

Recently, Sapra and Sarma[37] evaluated the electronic structure of II–VI semiconductor nanocrystals (between 5 and 80 Å) using a modified tight-binding model (TBM), developed by the same group, for bulk II–VI semicoductors.[38] The variations in the band gap difference between the nanocrystals and bulk crystals with the diameter of the nanocrystals were best fit to an empirical formula, $\Delta E_g = a_1 e^{-d/b_1} + a_2 e^{-d/b_2}$ (where ΔE_g is the difference between the band gaps of nanocrystals and bulk in eV, d is the diameter of nanocrystals in nm and a_1 = 2.83 and 7.44, a_2 = 1.96 and 3.04, b_1 = 8.22 and 2.35, and b_2 = 18.07 and 15.30 for CdS and ZnS, respectively).[37] Fig. 10(A) displays a plot of ΔE_g *versus* d for the CdS and ZnS nanocrystals using the above empirical

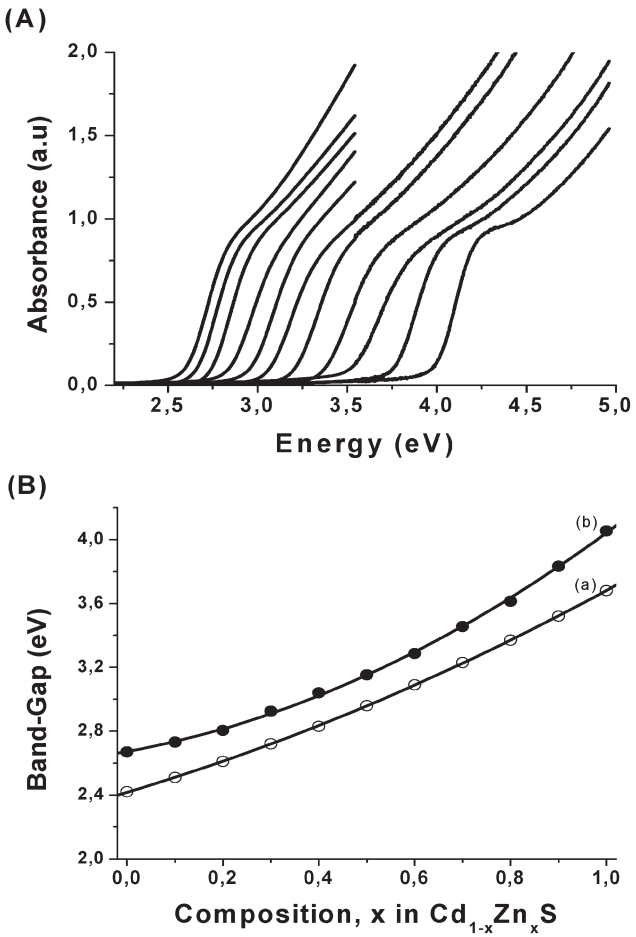

Fig. 9 (A) UV-Vis absorption spectra of $Cd_{1-x}Zn_xS$ nanocrystals in the mesostructured silica films (low energy end is pure CdS, high energy end is pure ZnS, the spectra in between the spectra of CdS and ZnS are from the $Cd_{1-x}Zn_xS$ nanocrystals, where x is increasing from 0.1 to 0.9 with an increment of 0.1 going from left to right). (B) Plots of band gap (E_g) *versus* x of (a) nano$Cd_{1-x}Zn_xS$–mesoSiO$_2$ and (b) bulk materials obtained from empirical formula given in reference 36.

formula. Notice that the variations in the band gap with respect to the particle size in both CdS and ZnS, are very similar. We assume that the variation in the nano$Cd_{1-x}Zn_xS$ will also follow the same trend, given in Fig. 10(A). The size of nano$Cd_{1-x}Zn_xS$ nanocrystals in mesoSiO$_2$ were evaluated using the plot in Fig. 10(A) and the ΔE_g was evaluated using the plots in Fig. 9(B). Fig. 10(B) displays the variation in the particle size of the nano$Cd_{1-x}Zn_xS$–mesoSiO$_2$ with x. Note that the variation in the particle size of our nanocrystals correlates with the observed deviation in the E_g *versus* x plots in Fig. 9(B). The CdS and ZnS nanoparticles are smaller but all the intermediate compositions have similar particle size, Fig. 10(B). Note also that the band gaps of the nanocrystals with intermediate compositions display an almost linear dependence (Vegard type plot) on the composition, indicating solid-solution behavior in nano$Cd_{1-x}Zn_xS$–mesoSiO$_2$.

The particle size of the nanocrystals were also evaluated using Scherrer's formula ($D = 0.9\lambda/B\cos\theta$, where D is the diameter of the particles in Å, λ is the wavelength of the X-ray source, 1.54078 Å, B is the corrected full width at half maximum in radians and θ is half of the angle of diffraction of the (111) plane) and the XRD patterns of thicker film samples of nano$Cd_{1-x}Zn_xS$–mesoSiO$_2$. The particle sizes of $Cd_{1-x}Zn_xS$ nanocrystals, obtained from Scherrer's formula, are around 4.0 nm, consistent with the values obtained from the band gap (using the relation obtained from TBM). The findings from the UV-Vis absorption spectroscopy, TEM and XRD techniques collectively show that a solid solution is forming in the nanocrystals of $Cd_{1-x}Zn_xS$ inside the channels of mesostructured silica.

The effect of aging the film samples was also investigated using UV-Vis spectroscopy after H_2S reaction. Trends in the UV-Vis absorption spectra of these samples also fall into two categories, fresh and aged. Fig. 11 displays UV-Vis absorption spectra of a fresh sample (aged for 15 minutes before the H_2S reaction) and two aged (one aged for 3 days at RT and another aged further at 240 °C for 45 minutes before H_2S reaction) samples after the H_2S reaction of the

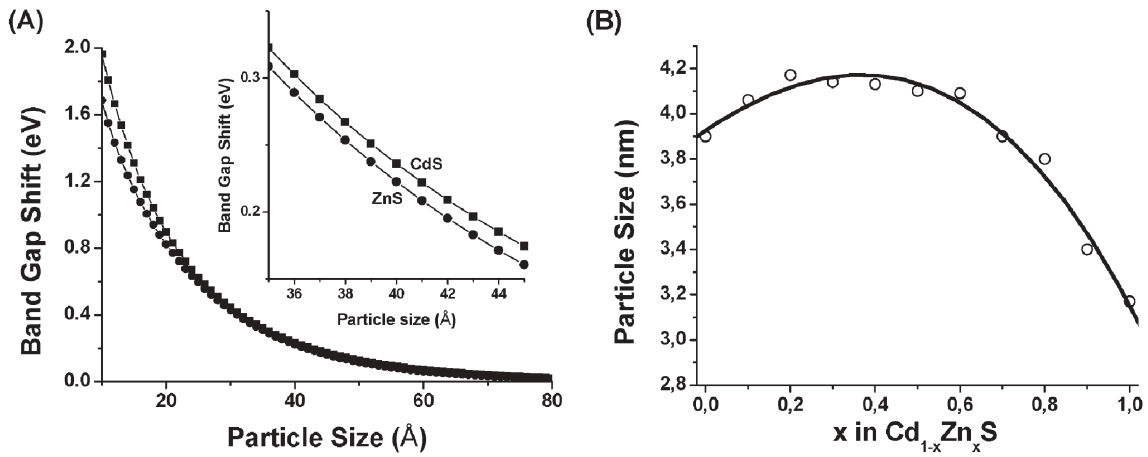

Fig. 10 (A) Plot of band gap shift (ΔE_g) of CdS and ZnS obtained from an empirical formula ($\Delta E_g = a_1e^{-d/b_1} + a_2e^{-d/b_2}$, where ΔE_g is the difference between the band gaps of nanocrystals and bulk in eV, d is the diameter of nanocrystals in nm and $a_1 = 2.83$ and 7.44, $a_2 = 1.96$ and 3.04, $b_1 = 8.22$ and 2.35, and $b_2 = 18.07$ and 15.30 for CdS and ZnS, respectively[37]). The inset is the same plot showing the regions used in this work. (B) Plot of particle size evaluated from the plot in (A) *versus* x in nano$Cd_{1-x}Zn_xS$–mesoSiO$_2$.

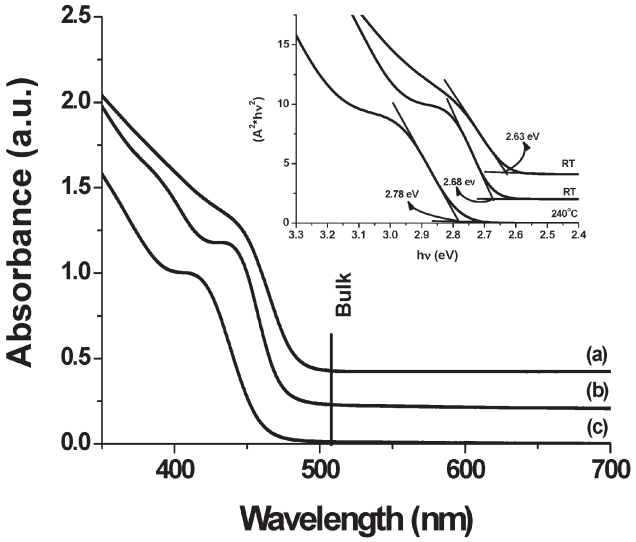

Fig. 11 The UV-Vis absorption spectra of H_2S treated films of $[Cd(H_2O)_4](NO_3)_2$–mesoSiO$_2$ ($Cd^{2+}/C_{12}EO_{10}$ ratio is 1.0 in all samples); (a) a relatively fresh film sample (aged for only 1 hour), (b) sample aged for 3 days, and (c) the 3 days aged sample after further aging at 240 °C. The inset is a plot of (Absorbance × Energy (eV))^2 *vs.* Energy (eV) of the three samples in (a), (b) and (c).

$[Cd(H_2O)_4](NO_3)_2$–mesoSiO$_2$. The optical band gaps of the nanoCdS–mesoSiO$_2$ shift from 2.63 eV (at RT) to 2.78 eV (at 240 °C), respectively, corresponding to 4.3 nm and 3.3 nm CdS nanoparticles, see inset in Fig. 11. Fig. 12 shows a series of absorption spectra recorded from the film samples aged at RT and 100 °C for different periods of time. In addition to a blue shift in the absorption edge, the spectrum of the aged sample displays a relatively sharp absorption edge with some structure (discrete like energy levels), indicating smaller particles and a uniform size distribution of the CdS nanoparticles in the aged silica channels. Notice that the prolonged heating at 100 °C causes broadening on the absorption edge, Fig. 12. The blue shift on the absorption edge, and the shift of the X-ray diffraction line with aging at RT and higher temperatures are consistent with each other, see Fig. 12 and 4, respectively. Therefore, the rigidity of the silica walls is important in the growth process and the size distribution of the $Cd_{1-x}Zn_xS$ nanoparticles in the channels of the mesostructured silica films. Both XRD patterns and UV-Vis absorption spectra indicate that the nanoparticles are relatively smaller in the aged matrix and have a more uniform size distribution. We are currently investigating the matrix effect of the growth, particle size and size distribution in a much softer environment, such as an LC mesophases of salt : C_nEO_m systems.[21]

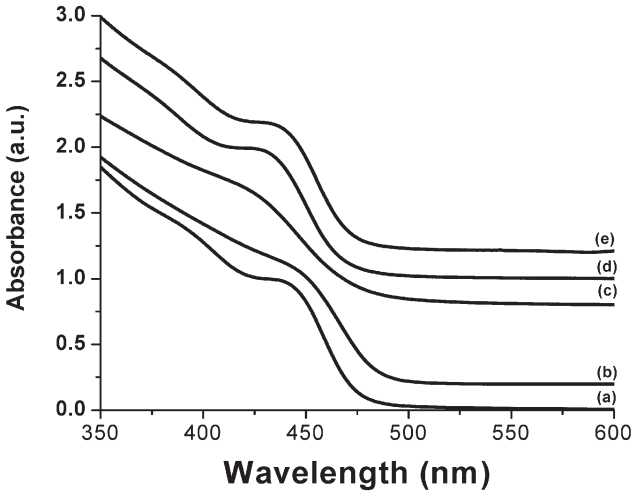

Fig. 12 The UV-Vis absorption spectra of the nanoCdS–mesoSiO$_2$ film samples that were aged before H_2S reaction at RT for (a) 2 days and (b) 30 minutes and at 100 °C for (c) 2 days, (d) 5 h, and (e) 30 minutes.

Conclusion

In this work, we have developed a new and simple method to produce $Cd_{1-x}Zn_xS$ nanocrystals in the channels of mesostructured silica. The Cd(II) and Zn(II) ions can be homogeneously incorporated into the channels of mesostructured silica thin films using the TLCT approach with the help of the MLC mesophase. Simply, preparing MLC mesophases with compositions of $(1-x)[Cd(H_2O)_4](NO_3)_2$ to $x[Zn(H_2O)_6](NO_3)_2$ mole ratio enables us to control: i) the homogeneous distribution of Cd^{2+} and Zn^{2+} ions in channels of the mesostructured silica films, ii) the composition of the $Cd_{1-x}Zn_xS$ nanoparticles after exposing the silica films to H_2S gas, and iii) tuning the optical band gap of the $Cd_{1-x}Zn_xS$ nanocrystals between 2.63 and 4.05 eV. Aging of the film samples has a strong impact on the growth process and size distribution of the nanocrystals. For example, the band gap of CdS nanoparticles can also be tuned between 2.63 and 2.78 eV by controlling the aging temperature and aging period of the $[Cd(H_2O)_4](NO_3)_2$–mesoSiO$_2$ film samples. Rigid silica walls of mesopores limit or stop the growth of the $Cd_{1-x}Zn_xS$ nanoparticles in the channels of mesostructured silica. The method described above could also be used to produce other alloy metal sulfides and metal selenides.

Acknowledgements

The authors would like to thank to Dr Marc Mamak for the TEM imaging and Mr Wes Whitnal for NMR measurements. For the financial support, ÖD gratefully acknowledges the Scientific and Technical Research Council of Turkey (TÜBİTAK) in the framework of the project TBAG-2263 (102T188), the Turkish Academy of Science in the framework of Young Scientist Award (ÖD/TÜBA-GEBİP/2002-1-6) and Bilkent University (CHEM-01-05).

References

1 C. T. Kresge, M. E. Leonowicz, W. J. Roth, J. C. Vartuli and J. S. Beck, *Nature*, 1992, **359**, 710.
2 P. T. Tanev, M. Chibwe and T. J. Pinnavaia, *Nature*, 1994, **368**, 321.
3 X. Feng, G. E. Fryxell, L. Q. Wang, A. Y. Kim, J. Liu and K. M. Kemner, *Science*, 1997, **276**, 923.
4 B. J. Scott, G. Wirnsberger and G. D. Stucky, *Chem. Mater.*, 2001, **13**, 3140.
5 S. H. Joo, S. J. Choi, I. Oh, J. Kwak, Z. Liu, O. Terasaki and R. Ryoo, *Nature*, 2001, **412**, 169.

6 W. H. Zhang, J. L. Shi, H. R. Chen, Z. L. Hua and D. S. Yan, *Chem. Mater.*, 2001, **13**, 648.
7 Ö. Dag, G. A. Ozin, H. Yang, C. Reber and G. Bussiere, *Adv. Mater.*, 1999, **11**, 474.
8 T. Hirai, H. Okubo and I. Komasawa, *J. Phys. Chem. B*, 1999, **103**, 4228.
9 S. Besson, T. Gacoin, C. Ricolleau, C. Jacquiod and J. P. Boilot, *Nano Lett.*, 2002, **2**, 409.
10 K. S. Morley, P. C. Marr, P. B. Webb, A. R. Berry, F. J. Allison, G. Moldovan, P. D. Brown and S. M. Howdle, *J. Mater. Chem.*, 2002, **12**, 1898.
11 G. S. Attard, J. C. Glyde and C. G. Göltner, *Nature*, 1995, **378**, 366.
12 C. Tura, N. Coombs and Ö. Dag, *Chem. Mater.*, 2005, **17**, 573.
13 J. Fan, C. Yu, F. Gao, J. Lei, B. Tain, L. Wang, Q. Luo, B. Tu, W. Zhou and D. Zhao, *Angew. Chem., Int. Ed.*, 2003, **42**, 3146.
14 Ö. Dag, O. Samarskaya, N. Coombs and G. A. Ozin, *J. Mater. Chem.*, 2003, **13**, 328.
15 X. Gao and S. Nie, *J. Phys. Chem. B*, 2003, **107**, 11575.
16 F. J. Brieler, P. Grundmann, M. Fröba, L. M. Chen, P. J. Klar, W. Heimbrodt, H. A. K. von Nidda, T. Kurz and A. Loidle, *J. Am. Chem. Soc.*, 2004, **126**, 797.
17 A. V. Kouzema, M. Fröba, L. Chen, P. J. Klar and W. Heimbrodt, *Adv. Funct. Mater.*, 2005, **15**, 168.
18 F. J. Brieler, P. Grundmann, M. Fröba, L. Chen, P. J. Klar, W. Heimbrodt, H. A. K. von Nidda, T. Kurz and A. Loidl, *Chem. Mater.*, 2005, **17**, 795.
19 P. V. Braun, P. Osenar and S. I. Stupp, *Nature*, 1996, **380**, 325.
20 X. Jiang, Y. Xie, J. Lu, L. Zhu, W. He and Y. Qian, *Chem. Mater.*, 2001, **13**, 1213.
21 Ö. Dag, S. Alayoğlu, C. Tura and Ö. Çelik, *Chem. Mater.*, 2003, **15**, 2711.
22 H. Luo, L. Sun, Y. Lu and Y. Yan, *Langmuir*, 2004, **20**, 10218.
23 Y. Yamauchi, T. Momma, T. Yokoshima, K. Kuroda and T. Osaka, *J. Mater. Chem.*, 2005, **15**, 1987.
24 Ö. Çelik and Ö. Dag, *Angew. Chem., Int. Ed.*, 2001, **40**, 3800.
25 Ö. Dag, S. Alayoğlu and İ. Uysal, *J. Phys. Chem. B*, 2004, **108**, 8439.
26 T. Taguchi, Y. Endoh and Y. Nozue, *Appl. Phys. Lett.*, 1991, **56**, 342.
27 S. Guha, B. J. Wu, H. Cheng and J. M. Depuydt, *Appl. Phys. Lett.*, 1993, **63**, 2129.
28 B. Bhattacharjee, S. K. Mandal, K. Chakrabarti, D. Ganguli and S. Chaudhuri, *J. Phys. D: Appl. Phys.*, 2002, **35**, 2636.
29 J. Cizeron and M. P. Pileni, *J. Phys. Chem.*, 1995, **99**, 17410.
30 X. Zhong, S. Liu, Z. Zhang, L. Li, Z. Wei and W. Knoll, *J. Mater. Chem.*, 2004, **14**, 2790.
31 W. Wang, I. Germanenko and M. S. El-Shall, *Chem. Mater.*, 2002, **14**, 3028.
32 A. P. Alivisatos, *Science*, 1996, **271**, 933.
33 H. Yang, N. Coombs, I. Sokolov and G. A. Ozin, *J. Mater. Chem.*, 1997, **7**, 1285.
34 X.-F. Zhou, C.-Z. Yu, J. W. Tang, X. X. Yan and D. Y. Zhao, *Microporous Mesoporous Mater.*, 2005, **79**, 283.
35 B. Donnio, B. Heinrich, H. Allouchi, J. Kain, S. Diele, D. Guillon and D. W. Bruce, *J. Am. Chem. Soc.*, 2004, **126**, 15258.
36 G. K. Padam, G. L. Malhotra and S. U. M. Rao, *J. Appl. Phys.*, 1988, **63**, 770.
37 S. Sapra and D. D. Sarma, *Phys. Rev. B*, 2004, **69**, 125304.
38 S. Sapra, N. Shanthi and D. D. Sarma, *Phys. Rev. B*, 2002, **66**, 205202.